# Analytic Approximation of High-Fidelity Solar Radiation Pressure

Yoshimura, Yasuhiro
Department of Aeronautics and Astronautics, Kyushu University : Professor

Matsushita, Yuri
Department of Aeronautics and Astronautics, Kyushu University : Assistant Professor

Takahashi, Kazunobu
Department of Aeronautics and Astronautics : Graduate Student

Nagasaki, Shuji
Department of Aeronautics and Astronautics : Graduate Student

他



出版情報：Journal of Guidance, Control, and Dynamics. 46 (1), pp.171-176, 2022-09-09. American Institute of Aeronautics and Astronautics
バージョン：
権利関係：

# In-situ 1-kHz real-time particle tracking velocimetry using high-speed streaming camera

Tenshiro Ichimura, Chihiro Inoue, Zhenying Wang[a], George Kuwabara[b], Kenji Tahara[c]

[a]*Department of Aeronautics and Astronautics, Kyushu University, 744 Moto-oka, Nishi-ku, Fukuoka, 819-0395, Japan*
[b]*Photron Ltd., Kanda, Jimbocho, Chiyoda-ku, Tokyo, 101-0051, Japan*
[c]*Department of Mechanical Engineering, Kyushu University, 744 Moto-oka, Nishi-ku, Fukuoka, 819-0395, Japan*

**Abstract**

This paper describes the use of a high-speed streaming camera combined with in-house image processing for real-time particle tracking velocimetry (PTV) above 1 kHz. The proposed system is evaluated by measuring the diameter and velocity of multiple free-falling droplets in a simultaneous manner. Two existing particle tracking methods are examined: median flow (MF) and four-frame best estimate (4BE). Area-limiting processing is newly added to MF and 4BE to reduce the region of interest (ROI) in which particles are detected in the next image, resulting in area-limiting MF (AMF) and area-limiting 4BE (A4BE). Except for MF, the rest three methods of AMF, 4BE, and A4BE are capable of 1-kHz real-time PTV for 1246 pixel × 600 pixel images, with 4BE and A4BE achieving even at 10 kHz for 1246 pixel × 100 pixel images. The processing times for the tracking and image preparation are measured, and the bottleneck is found to be the image acquisition and preparation, rather than the tracking. AMF achieves faster processing times than MF in all conditions, showing the effectiveness of the limited ROI, while 4BE and A4BE exhibit comparable performance. The measurement error is confirmed to be approximately 1% for the droplet velocity and diameter, demonstrating the high accuracy of the first in-situ real-time PTV exceeding 1 kHz.

*Keywords:* Particle tracking velocimetry, real-time measurement, high-speed streaming camera, droplet

## 1. Introduction

With the development of faster and smarter Internet-of-Things technologies, interest in real-time data processing is growing rapidly. This requires the analysis of data as soon as they are acquired for the output of useful results, such as for optimal marketing based on store sales data or the non-contact measurement of body surface temperatures [1, 2, 3, 4, 5]. The advantage of real-time data processing is that it allows decisions to be made instantly and future trends to be forecast promptly. For fluid devices, real-time measurements are expected to contribute to optimal printing using the real-time measured flow rate of ink in 3D bioprinters [6] and aerodynamic control by measuring the flow around wings [7]. Time- and space-resolved flow visualization [8] would provide an intuitive approach for real-time image processing, although the acquisition and analysis of large-scale image data must be improved. For tracking the droplets ejected when a human sneezes, in which the mean droplet velocity is 2–5.4 m/s [9] over a spreading distance of $O(10^{-1})$ m, it is necessary to capture images at 1 kHz. High-speed (HS) imaging above 1 kHz would be beneficial in clarifying the time-resolved multiphase flow dynamics. However, today's HS imaging is not a real-time measurement technique, in that downloading the recorded images from the camera memory to a computer takes much longer than the time-scale of the phenomenon, and so the image analysis can only be conducted after the phenomenon has finished. Recently, a HS streaming camera was developed that can record images at over 1 kHz and transfer them directly to a computer memory in a simultaneous manner, potentially allowing for the HS real-time measurement of multiphase flows.

The widely used non-contact method of particle image velocimetry (PIV) acquires the velocity distribution of small tracer particles following the fluid flow by applying cross-correlation to the deformation pattern of the particle group over the entire image [10]. Particle tracking velocimetry (PTV) uses magnified images to measure the velocity and size of individual particles, tracking the detected particles in an image through successive frames in a Lagrangian manner. As PTV directly measures the actual trajectory of particles, it is applicable to particle motions that exhibit sudden changes in direction [11]. However, PTV fails to match particles in consecutive images when displacement of particles is much larger than the distance to neighboring particles. Thus, PTV generally requires a high frame rate and low particle density [12]. Scharnowski and Kähler [13] reviewed several PTV techniques, including those based on the schlieren method [14, 15] and molecular tags [16]. Magnetic resonance velocimetry without particles has also been developed to analyze blood flow in animals and the human body [17], as well as to measure the 3D flow in the internal cooling channels of gas turbine blades [18] and predict residual materials in tanks after drainage [19].

Various effective algorithms for enhancing the analysis speed and accuracy of PTV have been developed [11, 20, 21]. Shaffer

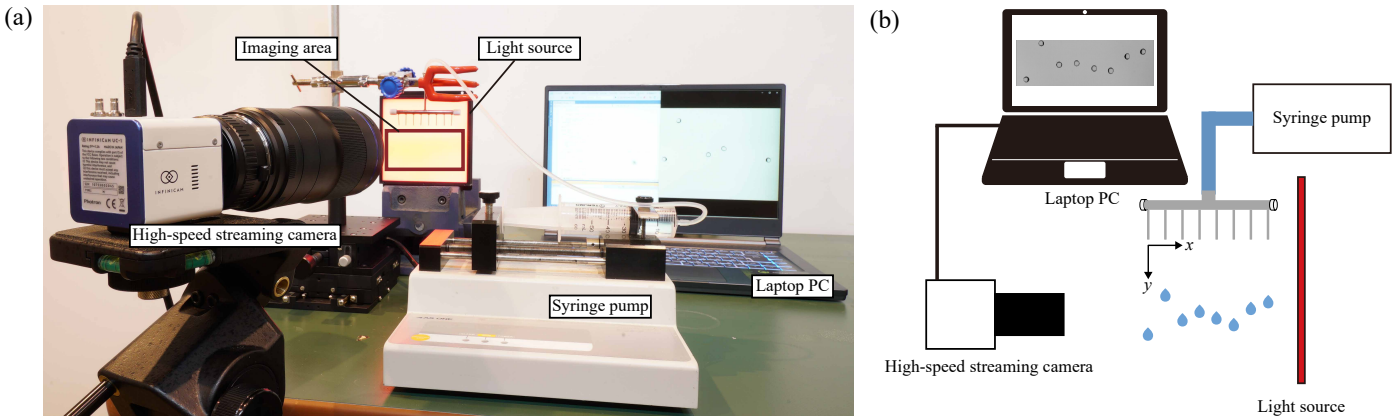


**Fig. 1.** Experimental setup: (a) photograph, (b) schematic diagram. Water is supplied from the syringe pump. The HS streaming camera is used to capture shadow images of free-falling droplets from the syringe tips. The captured images are transferred to the laptop by USB-C.

et al. developed a PTV method that directly measures trajectories with abrupt direction changes and strong recirculation, and applied this method to track tracer particles in jets with Reynolds numbers ranging from 1000–25000 [11]. Tirelli et al. proposed a high-resolution PTV tool considering uncertainty quantification [20] by employing a nonparametric supervised learning method [22]. Schanz et al. developed the Shake-the-Box method, which can identify and track up to hundreds of thousands of particles per time step. This enables the PTV processing of dense flows [21], which was previously limited to PIV evaluations such as TOMO-PIV [23, 24]. Lacassagne et al. used Shake-the-Box to perform 3D PTV measurements on oscillating-grid turbulent flows of dilute polymer solutions, and showed that the results were consistent with those from 2D PIV [25]. Eschner et al. constructed a system that measures the particle trajectories in a metal laser powder melting furnace using 3D PTV, and achieved a processing speed of 250 Hz by parallelizing the MATLAB code on a GPU [26]. Deng et al. constructed a method for simultaneously measuring the temperature and velocity components of particles in a microfluidic device at a processing rate of 10 Hz [27]. Guo et al. achieved real-time 3D-PTV at 30 Hz by performing tracking processing on a Field Programmable Gate Array (FPGA) [28]. Chan et al. developed an image compression algorithm for particle tracking on FPGA [29], and Kreizer et al. achieved 500 Hz real-time PTV for vortex flow by extracting particle-related information on FPGA [30].

Despite extensive studies in the past, there is currently no real-time PTV that achieves a processing rate exceeding 1 kHz, which is the rate necessary for the detection and control of fast multiphase flow fields. Therefore, this paper describes the use of a recently developed HS streaming camera for the development of real-time PTV above 1 kHz for the first time. We present the system setup and image analysis technique, and then demonstrate the 1-kHz real-time PTV for multiple falling droplets. The remainder of this paper is structured as follows. The experimental setup is introduced in Sec. 2, and then the image processing technique and associated PTV algorithm are presented in Sec. 3. The experimental results and a discussion of the processing time and measurement accuracy are given in Sec. 4. Finally, the conclusions are summarized in Sec. 5.

## 2. Experimental setup

As employed in previous researches[31, 32, 33], falling droplets have been widely used as a simple multiphase flow. Figure 1 shows an overview of the present experimental setup for multiple free-falling water droplets. The pump (AZ ONE SP-2PC) supplies water at a constant flow rate of 0.25 ml/s to the syringe through the tube. The syringe has eight ejection holes with outer diameters of 1 mm, lined horizontally every 9 mm. Up to eight water droplets fall simultaneously in the still air. The droplet diameter is $d$ = 3.0–3.1mm directly measured by the ImageJ software (Version 1.53t) [34]. We define the origin of the coordinate system as the tip of the syringe at the left end; the $x$-, $y$-axes are defined in the horizontal and vertical directions, respectively.

After the falling droplets reach the quasi-steady state, a HS streaming camera (Photron INFINICAM UC-1), connected to a LAOWA 100 mm f/2.8 2X Ultra Macro APO lens, records time-resolved backlight images uniformly illuminated by red light from an LED panel (Leimac IHMA-214/226RHV-V, see Appendix A). The INFINICAM is equipped with a fast-response complementary metal–oxide–semiconductor image sensor, capable of 1-kHz transmission of grayscale images with a size of $x \times y$ = 1246 pixel × 1008 pixel and a maximum of 30 kHz transmission of 1246 pixel × 16 pixel images. Thus, the horizontal resolution is fixed at 1246 pixels, while the vertical resolution decreases at higher frame rates. Through the USB-C cable, the captured 8-bit raw images, compressed in real time by FPGA implemented in the camera hardware, are sequentially transferred to the laptop (MSI Delta15), which is controlled by the Windows 11 operating system, to perform PTV analysis.

The PTV system illustrated in Fig. 1 is "isolated," *i.e.*, disconnected from an external supercomputer, so it is called an "in-situ" system, and is easily portable to other circumstances.

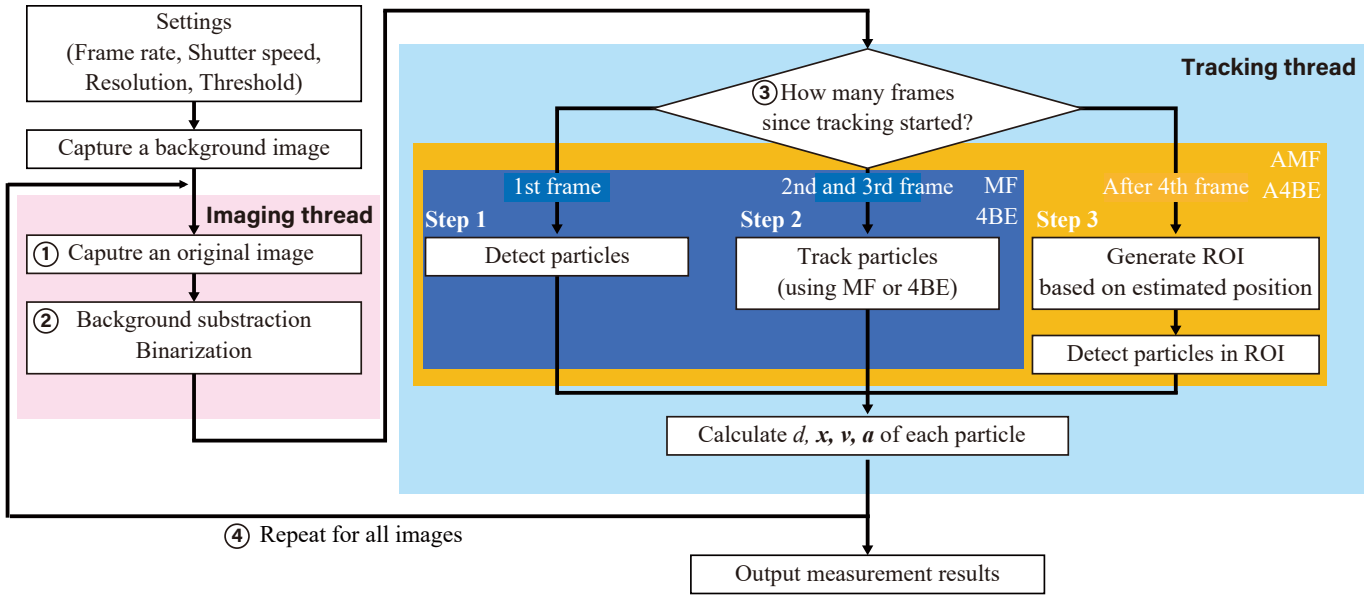


**Fig. 2.** Flowchart of proposed PTV algorithm. The algorithm uses multithread processing, with the *Imaging* thread on the red background performing the image acquisition and preparation, and the *Tracking* thread on the blue background performing the PTV processing.

## 3. PTV algorithm

The development environment of the present PTV algorithm is Microsoft Visual C++. OpenCV 4.5.2 is used as the image processing library. For the real-time PTV measurements, we examine the median flow (MF) [35] and four-frame best estimate (4BE) [36] methods. Two new methods are proposed by adding area-limiting processing to MF and 4BE, respectively, so as to reduce the region of interest (ROI) for particle detection in the next image. We refer to these newly developed methods as area-limiting MF (AMF) and area-limiting 4BE (A4BE).

### *3.1. Median Flow*

MF outputs a tracking rectangle $\beta_{n+1}$ containing the tracked tag points between two consecutive images, namely $I_n$ at frame $n$ and $I_{n+1}$ at frame $n+1$. The vector field indicating where the tag points are moving to is generated by the Lucas–Kanade tracker, which estimates the displacement of the tag points based on changes in the shading of the image. The displacement vector of the tracked object is determined by evaluating the forward–backward error and the normalized cross-correlation (NCC) [35]. In the present MF algorithm, we use the parameters provided by OpenCV, that is, pointsInGrid = 45, winSize = (3, 3), maxLevel = 7, maxCount = 20, epsilon = 0.01, winSizeNCC = (30, 30), and DisplacementDifference = 10.

### *3.2. Four-Frame Best Estimate*

4BE estimates the particle positions in image $I_{n+1}$ using images $I_{n-2}$, $I_{n-1}$, and $I_n$. Based on a particle's center of gravity $\boldsymbol{x}_{n-1}$, velocity $\boldsymbol{v}_{n-1} = (\boldsymbol{x}_n - \boldsymbol{x}_{n-1})/\Delta t$, and acceleration $\boldsymbol{a}_{n-1} = (\boldsymbol{v}_{n-1} - \boldsymbol{v}_{n-2})/\Delta t$ in image $I_{n-1}$, the estimated position $\bar{\boldsymbol{x}}_{n+1}$ is calculated by

$$\bar{\boldsymbol{x}}_{n+1} = \boldsymbol{x}_{n-1} + \boldsymbol{v}_{n-1}(2\Delta t) + \boldsymbol{a}_{n-1}\Delta t^2, \quad (1)$$

in which $\Delta t$ is the time between two frames [36]. The particle at $\boldsymbol{x}_{n+1}$ closest to $\bar{\boldsymbol{x}}_{n+1}$ is recognized as the same particle. 4BE requires at least three consecutive past images.

### *3.3. Area-Limiting ROI*

The proposed algorithm reduces the processing time by limiting the ROI for droplet detection. The limiting ROI technique in AMF and A4BE naturally assumes that the displacement of a particle is small between successive images, and is thus expected to work effectively with a HS streaming camera that acquires images at a high frame rate.

### *3.4. PTV Procedure*

Figure 2 depicts the image processing procedure. The PTV program employs multithread processing for the Imaging and Tracking threads.

In the Imaging thread, the processing is done as follows.

① We obtain a single image at the specified frame rate from the camera as a compressed raw image. An unzipped grayscale image is shown in Fig. 3(a).

② We subtract the pre-captured background image without the droplets from Fig. 3(a) to remove unnecessary information. We then convert the image to a binarized image, as shown in Fig. 3(b), in which the droplet edges are visible as circles on the black background. The binary threshold is set to 20.

In the corresponding Tracking thread, the processing can be described as follows.

③ The process is branched into three steps depending on the number of frames in which identical droplets are being tracked.

[Step 1] All objects in Fig. 3(b) are detected as particles including noise (even non-droplets). The objects are recognized

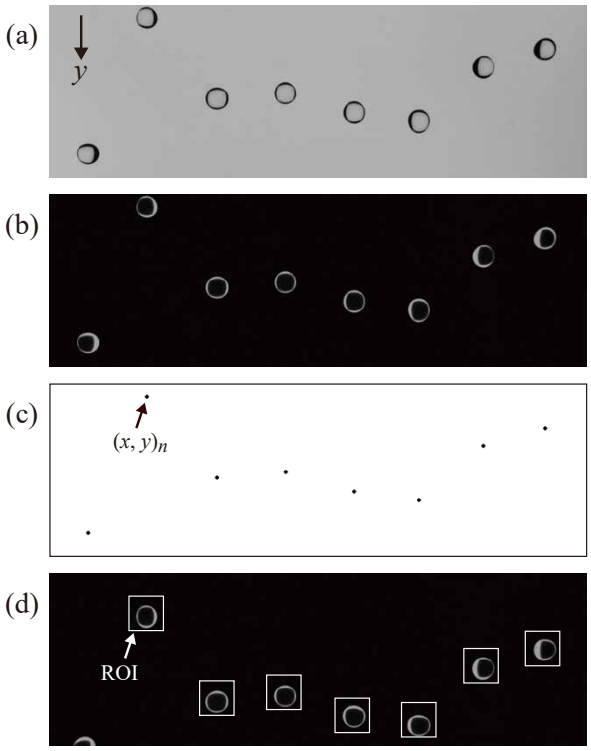


**Fig. 3.** Image processing of free-falling droplets. (a) Original image, (b) image with background subtracted, (c) distribution of droplet centers, (d) ROI for droplet tracking (white box indicates ROI).

as droplets when the projected area of an object $S$ in the image is greater than 10pixel$^2$. The geometric center $\boldsymbol{x_n} = (x, y)_n$ of each filled droplet is then calculated using the coordinate values $(x_i, y_i)$ and binarized brightness values $J(x_i, y_i)$ inside the droplet, wherein $J = 1$ is for pixels inside the droplet and $J = 0$ is for the outside.

$$(x, y)_n = \left( \frac{\sum_{x_i,y_i} x_i \cdot J(x_i, y_i)}{\sum_{x_i,y_i} J(x_i, y_i)}, \frac{\sum_{x_i,y_i} y_i \cdot J(x_i, y_i)}{\sum_{x_i,y_i} J(x_i, y_i)} \right)_n \tag{2}$$

Detected $\boldsymbol{x_n}$ is presented by the black points in Fig. 3(c).

[Step 2] In the first three frames after the start of tracking, the tracking process is performed by MF or 4BE. The initial diameter, position, velocity, and acceleration of each droplet are obtained, and the droplet position in the fourth and subsequent frames is estimated as in the original MF or 4BE.

[Step 3] When the area-limiting technique is adopted, the area around the estimated center of gravity of each droplet is defined as the ROI, as depicted in Fig. 3(d). The length of each side of the ROI is set as twice the droplet diameter obtained in Step 2. Center of the ROI is simply estimated by

$$\boldsymbol{x}_{n+1}^{\mathrm{ROI}} = \boldsymbol{x_n} + \boldsymbol{v_{n-1}} \Delta t. \tag{3}$$

AMF and A4BE search for droplets in the ROI, rather than in the entire image.

We measure the particle diameter $d$ as the area-equivalent diameter, $d = 2\sqrt{S/\pi}$. We finally update the droplet diameter, position, velocity, and acceleration, and repeat the process for the next image, as depicted by procedure ④.

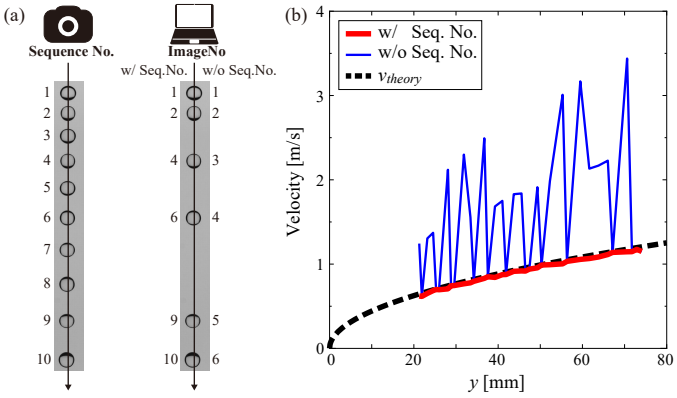


**Fig. 4.** Falling droplet velocity affected by missing images.

## 4. Results and discussion

To demonstrate real-time PTV above 1 kHz, we measure the velocity and size of multiple free-falling droplets using MF, 4BE, AMF, and A4BE. We also compare the measurement accuracy and processing speed.

### *4.1. Missing Images*

The HS streaming camera has a specific problem relating to quantitative image analysis. Despite widely used HS cameras (not streaming ones) having sufficient memory to record sequential images, they have limited memory, recording a single image and transferring it sequentially to the connected computer. As shown in Fig. 4(a), the HS streaming camera takes images at the specified frame rate with $f$ [Hz] and labels them sequentially with the number $N_s$ for the ten images from $N_s = 1$ to $N_s = 10$. When all images have been successfully transferred, the computer receives the ten images labeled from $N_s = 1$ to $N_s = 10$, and the time step of every image is naturally $\Delta t = 1/f$. However, when the computer fails to receive an image, *e.g.*, $N_s = 3$, the computer receives image $N_s = 4$, recognized as the third image. This missing image results in an incorrect time step being assumed between two subsequent frames. To solve this problem, we need to consider the sequential number on the computer and set the time step of $\Delta t_s = \Delta N_s / f$ instead of $\Delta t$. The following equation is then used to calculate the two-dimensional droplet velocity:

$$\boldsymbol{v_{n-1}} = \frac{\boldsymbol{x_n} - \boldsymbol{x_{n-1}}}{\Delta t_s}. \tag{4}$$

Figure 4(b) shows the results of absolute velocity measured by the 4BE tracking algorithm with and without considering the sequential number on the computer. When the sequential number is properly considered using the time step of $\Delta t_s$, the measured velocity profile is equivalent to the theoretical result, $v_{theory}$, for free-falling droplets accelerated by gravity as $v_{theory} = \sqrt{2gy}$, in which $g$ is the gravity acceleration. In contrast, when the sequence number is not taken into account, *i.e.*,

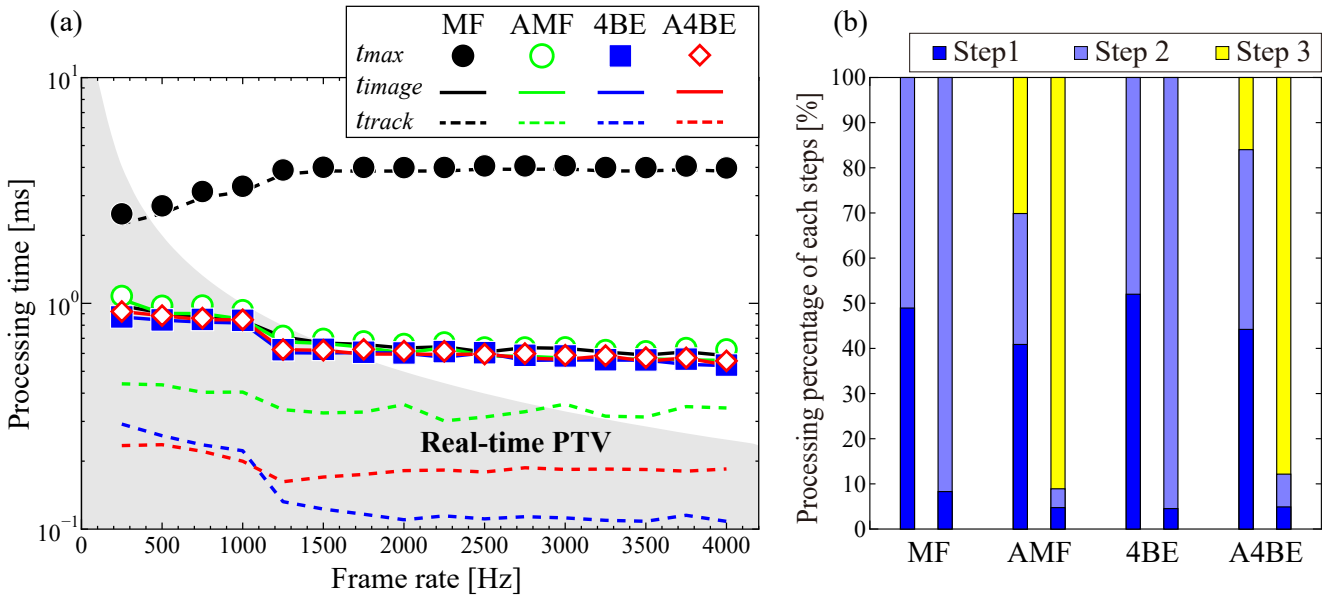


**Fig. 5.** Evidence of real-time PTV. (a) Processing time at various frame rates by the four methods. The gray area indicates the range where real-time measurements are realized. (b) Breakdown in the tracking thread (left: image capture at 1000 Hz, right: 4000 Hz).

**Table 1**
Experimental parameters

| | |
|---|---|
| Imaging frame rate | 250, 500, . . ., 4000 Hz |
| Vertical resolution | 96, 144, . . ., 1008 pixel |
| Number of tracked droplets | 1, 2, . . ., 8 |
| ROI size | 20, 40, . . ., 300 pixel |

employing the constant time step of $\Delta t$, the measurement results present unrealistic fluctuations because of the missing images. As the relationship between $\Delta t$ and $\Delta t_s$ is $\Delta t \leq \Delta t_s$, the velocity obtained without considering the sequential number overestimates the theoretical velocity. In the following analyses, we consistently consider the sequential number when measuring the velocity, as in Eq. (4).

### *4.2. Real-time PTV above 1 kHz*

We demonstrate real-time PTV above 1 kHz by examining the image processing time, which must be faster than the image recording time of $f^{-1}$ [s]. The average processing time per image is measured by varying the four parameters listed in Table 1: imaging frame rate, vertical resolution of an image, number of tracked droplets, and length of one side of the square ROI. We compare the results against reference values of 1000 Hz for the frame rate, 640 pixels for the vertical resolution, 8 tracked droplets, and a length of 100 pixels on one side of the ROI. As the present PTV algorithm employs multithread processing, we measure the processing times in both the Imaging thread, $t^n_{image}$, and the Tracking thread, $t^n_{track}$, and calculate their maximum value $t^n_{max}$ as the total processing time (not $t^n_{image} + t^n_{track}$) in image $I_n$. The mean values across $N = 5000$ images are calculated as follows:

$$t_{image} = \frac{\sum_N t^n_{image}}{N}, \tag{5}$$

$$t_{track} = \frac{\sum_N t^n_{track}}{N}, \tag{6}$$

$$t_{max} = \frac{\sum_N t^n_{max}}{N} = \frac{\sum_N \max(t^n_{image}, t^n_{track})}{N}. \tag{7}$$

Figure 5 shows the total processing time required to measure the velocity and size of falling droplets at various imaging frame rates. Real-time PTV is achieved at $t_{max} \leq f^{-1}$, as depicted by the gray area in Fig. 5(a). At the present image resolution of $x \times y = 1246 \times 640\text{pixel}^2$, 1-kHz real-time PTV is achieved by the three tracking algorithms of AMF, 4BE, and A4BE. The processing times for $t_{track}$ of 4BE and A4BE are much faster than those of MF and AMF. As the frame rate increases, the processing times of AMF becomes faster than that of MF. In contrast, the processing times of 4BE and A4BE remain equivalent. The processing time for $t_{image}$ is independent of the PTV tracking algorithm, and is therefore identical for all four algorithms (see also Fig. 2). For 4BE and A4BE, it is surprising to find that the tracking time is sufficiently fast that $t_{max} \approx t_{image}$. For MF and AMF, however, the tracking time is longer, constituting a large part of $t_{max}$. Typically, for MF, we notice $t_{max} \approx t_{track}$.

Figure 5(b) shows a breakdown of $t_{track}$ as the ratio of the steps constituting the Tracking thread, as depicted in Fig. 2. For MF and 4BE, this is Step 1 and Step 2; for AMF and A4BE, this is Steps 1–3. We compare frame rates of 1000 Hz and 4000 Hz while keeping the other conditions fixed. For MF and 4BE, the ratio of Step 2 rapidly increases and the ratio of Step 1 decreases as the frame rate increases. Considering a falling droplet, the

total frame number for tracking the droplet naturally increases as the imaging frame rate increases, indicating that the tracking process of Step 2 becomes dominant over the detection process of Step 1, which is only required once for each droplet. In the AMF and A4BE algorithms, the ratio of Step 3 increases remarkably, while the ratios of Steps 1 and 2 decrease. At high frame rate, generating the ROI for each droplet takes longer time than the processing time for tracking droplets. As the sequential images captured at the faster frame rate provide smaller droplet displacements, it is easy to identify the same droplet in the next frame. Regarding the tracking thread, MF is sufficiently "slow" and AMF effectively limits the tracking area, while 4BE is "fast" and the additional area-limiting process of A4BE is not beneficial, as confirmed in Fig. 5(a). To further accelerate the PTV system using 4BE and A4BE, $t_{image}$ must be shortened as a pre-conditioning step.

As the image size becomes larger, the processing time takes longer [Fig. 6(a)]. MF does not achieve 1-kHz real-time PTV unless the vertical resolution is less than 100 pixels, while AMF, 4BE, and A4BE successfully realize 1-kHz PTV up to 640-pixel resolution. We confirm that 4BE and A4BE realize real-time PTV at approximately 10 kHz for 1246 pixel × 100 pixel images. As shown in Fig. 6(b), when the number of tracked droplets changes, there is no significant difference in $t_{max}$ up to the maximum of eight droplets. Figure 6(c) shows that $t_{max}$ does not change when the ROI size changes. Thus, area-limiting method is a cost effective approach in a case that the tracking time takes long as in MF.

### 4.3. Measurement Accuracy

We now measure the velocity and diameter of the free-falling droplets at the spatial resolution of 60$\mu$m/pixel and imaging frame rate of 1 kHz. Figure 7 shows the measurement errors for time-varying velocity of a single droplet. The measurement results are compared with the theoretical results of $v_{theory}$. For a quantitative discussion, we define the measurement error of velocity, $\varepsilon_v$, as

$$\varepsilon_v = \frac{\sum_N |1 - \frac{v_{measure}}{v_{theory}}|}{N}, \tag{8}$$

where $v_{measure}$ denotes the measured value. During the free-fall motion of a droplet across an image area, a total of $N$ images are analyzed. The MF and AMF algorithm reproduces the theoretical result to within 5% and 2%, respectively. We confirm that 4BE and A4BE algorithms show $\varepsilon_v \approx 1\%$, demonstrating the high-accuracy of the present PTV measurement.

The measured velocity by A4BE algorithm exhibits fluctuations in Fig. 7. Figure 8 shows the time-varying aspect ratio of the droplet, which is defined as the ratio of vertical diameter to lateral diameter, and the difference between the measured and theoretical velocities. After leaving the syringe and starting to fall, the droplet periodically deforms with an approximate period of 20 ms, which corresponds to the capillary time scale of $\tau_\sigma \sim \sqrt{(\rho d^3/\sigma)} \approx 20$ms with a water density of $\rho = 10^3$kg/m$^3$, $d \approx 3$mm, and a surface tension coefficient of $\sigma = 0.07$N/m.

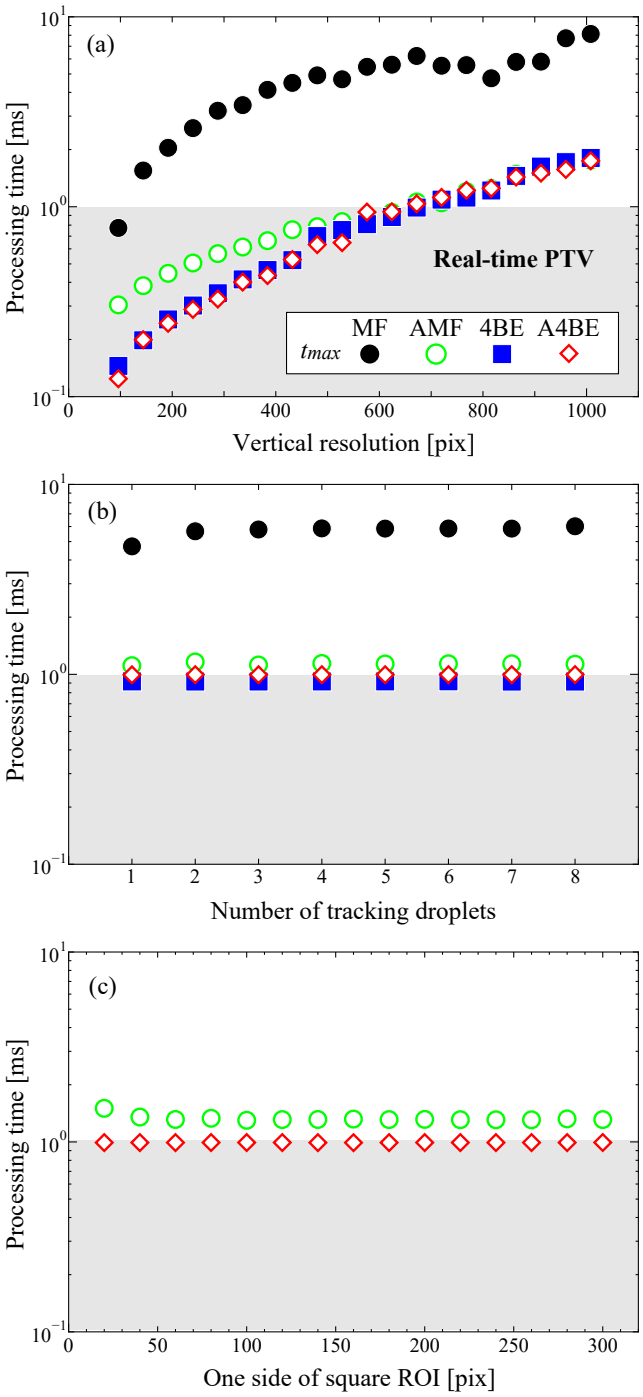


**Fig. 6.** Processing time (a) at various vertical resolutions, (b) with different number of tracked droplets, and (c) at various ROI sizes.

As visible in Fig. 3(b), the droplets are not perfectly spherical in shape and are slightly eccentric, resulting in fluctuations in the measured velocity calculated from the displacement of the center of gravity. Although the velocity difference is not completely synchronized with the aspect ratio, we can confirm similar trends between the aspect ratio and the velocity difference. Therefore, we consider the velocity fluctuations shown in Fig. 7 to be attributable to the droplet deformation, rather than the PTV algorithm.

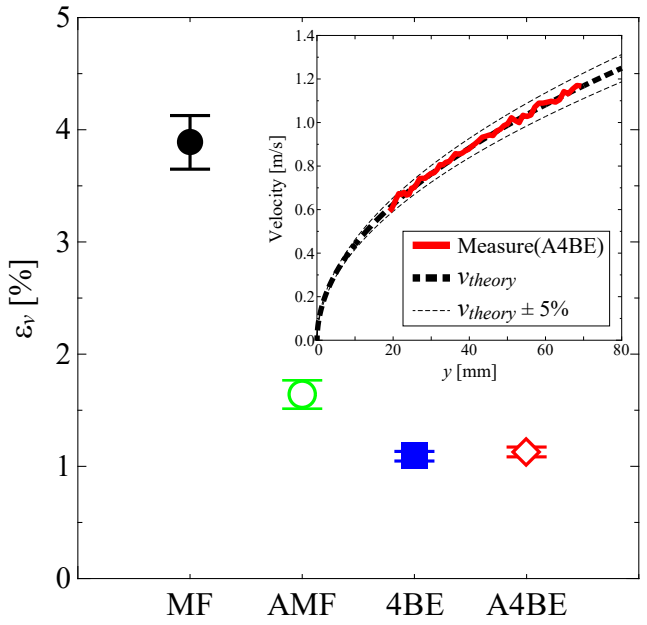


**Fig. 7.** Measurement errors for velocity of a falling droplet using the four different methods.

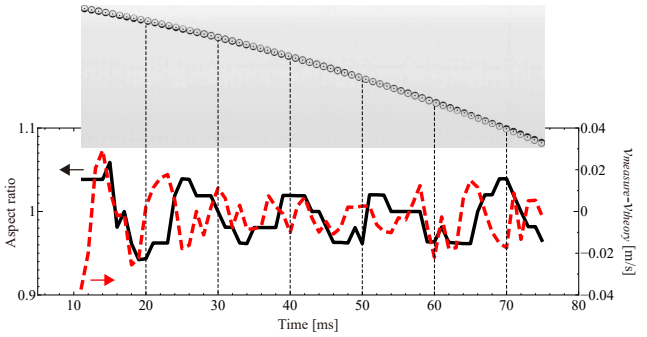


**Fig. 8.** Deformation of a free-falling droplet.

Figure 9 shows the measurement results of droplet diameter of 1000 droplets, $d_{measure}$, compared with the reference results directly obtained by the ImageJ software, denoted as $d_{imagej}$. The measurement error of the droplet size, $\varepsilon_d$, is calculated as

$$\varepsilon_d = \frac{\sum_N |1 - \frac{d_{measure}}{d_{imagej}}|}{N}. \tag{9}$$

We confirm that 4BE and A4BE algorithms demonstrate high accuracy of $\varepsilon_d \approx 1\%$. The A4BE algorithm well-reproduces the droplet size distribution of the ImageJ results. Therefore, the developed PTV system, including the experimental setup and PTV algorithm, is applicable for analyzing time- and space-resolved droplet dynamics with high accuracy.

## 5. Conclusion

We have developed a HS real-time PTV system using a HS streaming camera, allowing the velocity and size of droplets in multiphase flow to be measured in real time above 1 kHz, which

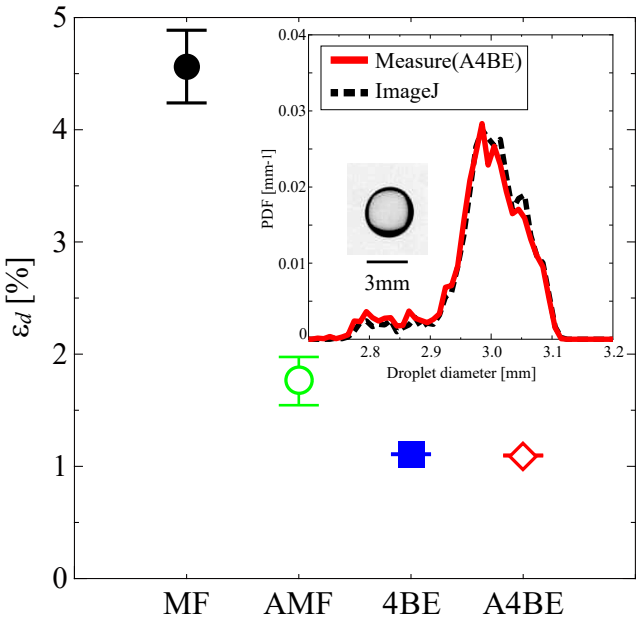


**Fig. 9.** Measurement errors for diameter of 1000 droplets.

was demonstrated by applying to multiple free-falling droplets. A new PTV algorithm was implemented to the existing MF and 4BE methods to reduce the tracking area, resulting in AMF and A4BE. Except for MF, the other three methods of AMF, 4BE, and A4BE were capable of 1-kHz real-time PTV for 1246 pixel $\times$ 600 pixel images, with 4BE and A4BE achieving even at 10 kHz for 1246 pixel $\times$ 100 pixel images. A comparison of MF and AMF showed that AMF had a shorter processing time than MF in all conditions, indicating the usefulness of limiting the particle detection area. 4BE and A4BE achieved similar performance, with no significant differences observed. The processing time in the tracking and image preparation processes was respectively measured. The bottleneck was found to be the image acquisition and preparation processes, not the tracking process. We confirmed the importance to adopt appropriate time increments by considering missing images that were not transferred to the laptop from the camera. The measurement error was approximately 1% for the droplet velocity and diameter, successfully demonstrating the high accuracy of the first in-situ real-time PTV system exceeding 1 kHz. The error was attributed to the deformation of falling droplets by capillarity.

The present framework has potential applications for real-time measurement of droplet velocity and size of practical sprays including a large number of spreading droplets (see Appendix B), tracking bubbles, and image-based inspection for all products flowing on a line, etc. Effective use of GPUs and FPGAs to accelerate the image acquisition and preparation processes could further improve the real-time PTV analysis.

## Acknowledgments

This study was supported by a grant for pioneering new engineering fields in Kyushu University.

## Appendix A

Figure 10(a) shows a distribution of the background brightness illuminated by the LED panel with no droplets, captured by the HS streaming camera at the shutter speed of 1 ms for 1246 pixel × 640 pixel. We confirm the uniformity across the entire image. The time variation of mean brightness shown in Fig. 10(b) conveys that there is a small fluctuation, less than unity (approximately 0.2) in 8-bit tones. By using the LED panel, uniform and stable backlit is provided, which is beneficial for analyzing the shadow images of droplets.

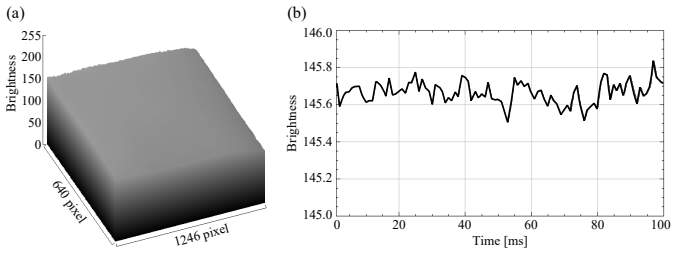


**Fig. 10.** The LED panel provides uniform brightness in space and time. (a) Brightness distribution of background image. (b) Time-variant brightness of the mean value in the whole pixels.

## Appendix B

The developed PTV system was applied to a spray spreading in 2D plane. Figure 11(a) shows the droplets being tracked. The blue rectangles indicate the detected droplets (not ROIs), and the red arrows depict the velocity vectors. Most droplets in the spray are tracked correctly. Similar to other 2D PTVs in general, it is difficult to track blurred droplets and overlapping ones. Figures 11(b)(c) present the distributions of droplet diameter and velocity, continuously measured for 70 ms. The present PTV system is capable of accumulating sufficient amount of data in a short period of time to perform statistical analysis.

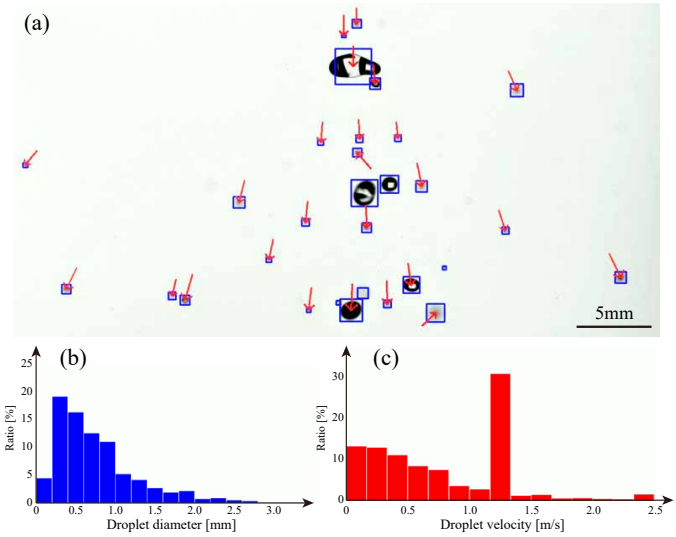


**Fig. 11.** Application of the developed PTV system to a 2D spray. (a) Instantaneous image overlapped with the detected droplets and their velocity vectors. (b) Droplet size distribution. (c) Droplet velocity distribution.

## References


[1] N. Li, C. Gong, D. Lv, Real-time prediction of cross-border e-commerce spike performance based on neural network and decision tree, Wirel. Commun. Mobile Comput. 2022 (2022) 5066467. doi:10.1155/2022/5066467.

[2] P. Escobedo, M. Fernández-Ramos, N. López-Ruiz, O. Moyano-Rodríguez, A. Martínez-Olmos, I. Pérez de Vargas-Sansalvador, M. Carvajal, L. Capitán-Vallvey, A. Palma, Smart facemask for wireless CO2 monitoring, Nat. Commun. 13 (1) (2022) 1–12. doi:10.1038/s41467-021-27733-3.

[3] A. Kuś, Real-time, multiplexed holographic tomography, Optics Lasers Eng. 149 (2022) 106783. doi:10.1016/j.optlaseng.2021.106783.

[4] F. K. Moghadam, A. R. Nejad, Online condition monitoring of floating wind turbines drivetrain by means of digital twin, Mech. Syst. Signal Process. 162 (2022) 108087. doi:10.1016/j.ymssp.2021.108087.

[5] S. Lyra, J. Rixen, K. Heimann, S. Karthik, J. Joseph, K. Jayaraman, T. Orlikowsky, M. Sivaprakasam, S. Leonhardt, C. Hoog Antink, Camera fusion for real-time temperature monitoring of neonates using deep learning, Med. Biol. Eng. Comput. 60 (6) (2022) 1787–1800.

[6] L. Wenger, S. Strauß, J. Hubbuch, Automated and dynamic extrusion pressure adjustment based on real-time flow rate measurements for precise ink dispensing in 3D bioprinting, Bioprinting 28 (2022) e00229. doi:10.1016/j.bprint.2022.e00229.

[7] N. Kanda, K. Nakai, Y. Saito, T. Nonomura, K. Asai, Feasibility study on real-time observation of flow velocity field using sparse processing particle image velocimetry, Trans. Jpn. Soc. Aeronaut. Space Sci. 64 (4) (2021) 242–245. doi:10.2322/tjsass.64.242.

[8] A. Etminan, Y. S. Muzychka, K. Pope, B. Nyantekyi-Kwakye, Flow visualization: state-of-the-art development of micro-particle image velocimetry, Meas. Sci. Technol. 33 (9) (2022) 092002. doi:10.1088/1361-6501/ac75b0.

[9] P. Bahl, C. de Silva, C. R. MacIntyre, S. Bhattacharjee, A. A. Chughtai, C. Doolan, Flow dynamics of droplets expelled during sneezing, Phys. Fluids 33 (11) (2021) 111901. doi:10.1063/5.0067609.

[10] T. Janke, R. Schwarze, K. Bauer, Part2track: a Matlab package for double frame and time resolved particle tracking velocimetry, SoftwareX 11 (2020) 100413. doi:10.1016/j.softx.2020.100413.

[11] F. Shaffer, E. Ibarra, Ö. Savaş, Visualization of submerged turbulent jets using particle tracking velocimetry, J. Vis. 24 (4) (2021) 699–710. doi:10.1007/s12650-021-00744-4.

[12] J. Heyman, TracTrac: A fast multi-object tracking algorithm for motion estimation, Comput. Geosci. 128 (2019) 11–18. doi:10.1016/j.cageo.2019.03.007.

[13] S. Scharnowski, C. J. Kähler, Particle image velocimetry–Classical operating rules from today's perspective, Optics Lasers Eng. 135 (2020) 106185. doi:10.1016/j.optlaseng.2020.106185.

[14] M. Yeganeh, Q. Cheng, A. Dharamsi, S. Karimkashi, J. Kuusela-Opas, O. Kaario, M. Larmi, Visualization and comparison of methane and hydrogen jet dynamics using schlieren imaging, Fuel 331 (2023) 125762. doi:10.1016/j.fuel.2022.125762.

[15] R. Kaufmann, S. N. Olufsen, E. Fagerholt, V. Aune, Reconstruction of surface pressures on flat plates impacted by blast waves using the virtual fields method, Int. J. Impact Eng. 171 (2023) 104369. doi:10.1016/j.ijimpeng.2022.104369.

[16] L. M. Vialta, P. A. de Souza Matos, L. G. Barreta, D. C. Junior, Methodology for the application of velocimetry by molecular tagging of hypersonic flows, Flow Meas. Instrum. (2022) 102265doi:10.1016/j.flowmeasinst.2022.102265.

[17] C. J. Elkins, M. T. Alley, Magnetic resonance velocimetry: applications of magnetic resonance imaging in the measurement of fluid motion, Exp. Fluids 43 (6) (2007) 823–858. doi:10.1007/s00348-007-0383-2.

[18] S. Baek, D. Kook, C. Kim, M. Bang, W. Hwang, Investigation of the relationship between the 3D flow structure and surface heat transfer within a realistic gas turbine blade trailing edge internal serpentine cooling channel, Int. J. Heat Mass Transf. 198 (2022) 123357. doi:10.1016/j.ijheatmasstransfer.2022.123357.

[19] A. Potanin, N. C. Shapley, Heel estimate during pressure-driven

drainage of gels from tanks, Chem. Eng. Sci. 230 (2021) 116158. doi:10.1016/j.ces.2020.116158.
[20] I. Tirelli, A. Ianiro, S. Discetti, An end-to-end KNN-based PTV approach for high-resolution measurements and uncertainty quantification, Exp. Therm. Fluid Sci. 140 (2023) 110756. doi:10.1016/j.expthermflusci.2022.110756.
[21] D. Schanz, S. Gesemann, A. Schröder, Shake-the-Box: Lagrangian particle tracking at high particle image densities, Exp. Fluids 57 (5) (2016) 1–27. doi:10.1007/s00348-016-2157-1.
[22] E. Fix, J. L. Hodges, Discriminatory analysis. Nonparametric discrimination: Consistency properties, Int. Stat. Rev./Revue Internationale de Statistique 57 (3) (1989) 238–247. doi:10.2307/1403797.
[23] G. E. Elsinga, F. Scarano, B. Wieneke, B. W. van Oudheusden, Tomographic particle image velocimetry, Exp. Fluids 41 (6) (2006) 933–947. doi:10.1007/s00348-006-0212-z.
[24] F. Scarano, Tomographic PIV: principles and practice, Meas. Sci. Technol. 24 (1) (2012) 012001. doi:10.1088/0957-0233/24/1/012001.
[25] T. Lacassagne, J. Vatteville, C. Degouet, M. El Hajem, S. Simoëns, PTV measurements of oscillating grid turbulence in water and polymer solutions, Exp. Fluids 61 (7) (2020) 1–15. doi:10.1007/s00348-020-03000-x.
[26] E. Eschner, T. Staudt, M. Schmidt, 3D particle tracking velocimetry for the determination of temporally resolved particle trajectories within laser powder bed fusion of metals, Int. J. Extrem. Manuf. 1 (3) (2019) 035002. doi:10.1088/2631-7990/ab3de9.
[27] Z. Deng, J. König, C. Cierpka, A combined velocity and temperature measurement with an LED and a low-speed camera, Meas. Sci. Technol. 33 (11) (2022) 115301. doi:10.1088/1361-6501/ac82da.
[28] R. Guo, E. Dekneuvel, G. Jacquemod, P. H. Biwole, A system-level description of a particle tracking velocimetry system for indoor air quality study, Science Talks 5 (2023) 100099. doi:10.1016/j.sctalk.2022.100099.
[29] K.-Y. Chan, D. Stich, G. A. Voth, Real-time image compression for high-speed particle tracking, Rev. Sci. Instrum. 78 (2) (2007) 023704. doi:10.1063/1.2536719.
[30] M. Kreizer, D. Ratner, A. Liberzon, Real-time image processing for particle tracking velocimetry, Exp. Fluids 48 (2010) 105–110. doi:10.1007/s00348-009-0715-5.
[31] F. Okino, K. Noborio, Y. Yamamoto, S. Konishi, Vacuum sieve tray for tritium extraction from liquid Pb–17Li, Fusion Eng. Des. 87 (7-8) (2012) 1014–1018. doi:10.1016/j.fusengdes.2012.02.071.
[32] M. Fernández-Raga, M. Cabeza-Ortega, V. González-Castro, P. Peters, M. Commelin, J. Campo, The use of high-speed cameras as a tool for the characterization of raindrops in splash laboratory studies, Water 13 (20) (2021) 2851. doi:10.3390/w13202851.
[33] N. Liu, X. Sheng, M. Zhang, W. Han, K. Wang, Squeeze-type piezoelectric inkjet printhead actuating waveform design method based on numerical simulation and experiment, Micromachines 13 (10) (2022) 1695. doi:10.3390/mi13101695.
[34] C. A. Schneider, W. S. Rasband, K. W. Eliceiri, NIH image to ImageJ: 25 years of image analysis, Nat. Methods 9 (7) (2012) 671–675. doi:10.1038/nmeth.2089.
[35] Z. Kalal, K. Mikolajczyk, J. Matas, Forward-backward error: Automatic detection of tracking failures, in: 2010 20th International Conference on Pattern Recognition, IEEE, 2010, pp. 2756–2759. doi:10.1109/ICPR.2010.675.
[36] A. Clark, N. Machicoane, A. Aliseda, A quantitative study of track initialization of the four-frame best estimate algorithm for three-dimensional Lagrangian particle tracking, Meas. Sci. Technol. 30 (4) (2019) 045302. doi:10.1088/1361-6501/ab0786.